Heusler compounds with perpendicular magnetic anisotropy and large tunneling magnetoresistance

Sergey V. Faleev, Yari Ferrante, Jaewoo Jeong, Mahesh G. Samant, Barbara Jones, and Stuart S. P. Parkin

Phys. Rev. Materials **1**, 024402 — Published 5 July 2017

DOI: 10.1103/PhysRevMaterials.1.024402

Heusler compounds with perpendicular magnetic anisotropy and large tunneling magnetoresistance

Sergey V. Faleev,[1,*] Yari Ferrante,[1,2,3] Jaewoo Jeong,[1] Mahesh G. Samant,[1] Barbara Jones,[1] and Stuart S. P. Parkin[1,3,†]

[1]*IBM Research - Almaden, 650 Harry Road, San Jose, California 95120, USA*
[2]*Martin Luther University, 06099 Halle (Saale), Germany*
[3]*Max Planck Institute for Microstructure Physics, 06120 Halle (Saale), Germany*

(Dated: May 29, 2017)

In present work we suggest a receipt for finding tetragonal Heusler compounds with perpendicular magnetic anisotropy (PMA) that also exhibit large tunneling magnetoresistance (TMR) when used as electrodes in magnetic tunnel junction (MTJ) devices with suitable tunneling barrier materials. We performed the density-functional theory calculations for 286 Heusler compounds and identified 116 stable tetragonal compounds. Ten of these compounds are predicted to have strong PMA and, simultaneously, exponentially increasing TMR with increasing tunneling barrier thickness due to the so-called Brillouin zone spin filtering effect. Experimental measurements performed for 25 Heusler compounds theoretically identified as tetragonal show that 10 of these compounds indeed have tetragonal structure with PMA. Eight of these compounds are reported for the first time.

PACS numbers: 73.40.Rw, 85.75.-d

I. INTRODUCTION

Key to the successful development of spin-transfer torque magnetic random access memory (STT-MRAM), one of the most promising emerging non-volatile memory technologies today, are new magnetic materials for MTJ memory elements that have sufficient stability against thermal fluctuations to sustain deeply scaled devices. The magnetic electrodes must possess sufficient PMA that their magnetizations lie perpendicular to the plane of the MTJ device, since this allows for reduced currents to switch the magnetization of the electrode that forms the memory layer of the device using spin torque[1,2]. The most promising magnetic materials to date are considered to be alloys formed from Co, Fe and B, in conjunction with MgO tunnel barriers[1,3,4]. Unfortunately, PMA of CoFeB layers arises from the interfaces between these layers and the tunnel barrier and/or underlayer and is too weak to overcome thermal fluctuations when the device has a critical dimension $\lesssim$ 20nm.

Magnetic materials in which the PMA is derived from volume magnetocrystalline anisotropy (MCA) are then needed. One of the most promising class of such materials are the Heusler alloys - compounds having the chemical formula X_2YZ wherein X and Y are transition metals, or lanthanides (rare-earth metals), and Z is the main group element[5]. While the parent Heusler compounds are cubic and do not exhibit magnetic anisotropy, the structure of some of these compounds is found to be tetragonally distorted and thus could potentially have large PMA.

Some examples of tetragonal Heusler compounds are $Mn_{3-x}Ga$[6] and Mn_3Ge[7]. Thin films of these materials have been shown to exhibit large PMA for films grown epitaxially on single crystalline substrates such as SrTiO3(001) or MgO(001)[7–11] and on amorphous substrates (Si(001)/SiO_2)[12]. Unfortunately, the experimental values of the tunneling magnetoresistance (TMR) for MTJs with $Mn_{3-x}Ga$ or Mn_3Ge electrodes and MgO spacer was found very small, far below the application range[12].

The goal of present paper is to identify promising tetragonal Heusler compounds that possess PMA and exhibit high TMR ether due to large spin polarization of bulk Heusler compound or due to the so-called Brillouin zone (BZ) spin filtering effect[13] for the MTJ with suitable spacer. Realization of the high TMR in a MTJ system with electrodes that have low crystal symmetry where PMA could be simultaneously achieved is of significant technological interest for spintronics applications, and, in particular, in the context of novel STT-MRAM technology that has a potential to become an 'universal memory'[14] combining all the strengths and none of the weaknesses of existing memory types.

II. THEORETICAL SEARCH FOR TETRAGONAL HEUSLER COMPOUNDS WITH PMA AND LARGE TMR

A. Crystal structure

Cubic Heusler compounds X_2YZ can have *regular* structure or *inverse* structure. These two crystal structures are shown in Fig. 1(a) and (c) with four sites forming four fcc sublattices: site Z (occupied by atom Z), site II, octahedrally coordinated by Z, and two equivalent sites I tetrahedrally coordinated by Z. In regular structure shown on Fig 1(a) two X atoms [red, labeled as X(I)] have identical environment - they are located on sites I in the same xy-plane. In this structure the Y atom (cyan) on site II and Z atom (grey) are located in another xy-plane. In inverse structure shown on Fig 1(c) two X atoms have different environment - one X atom [red, la-

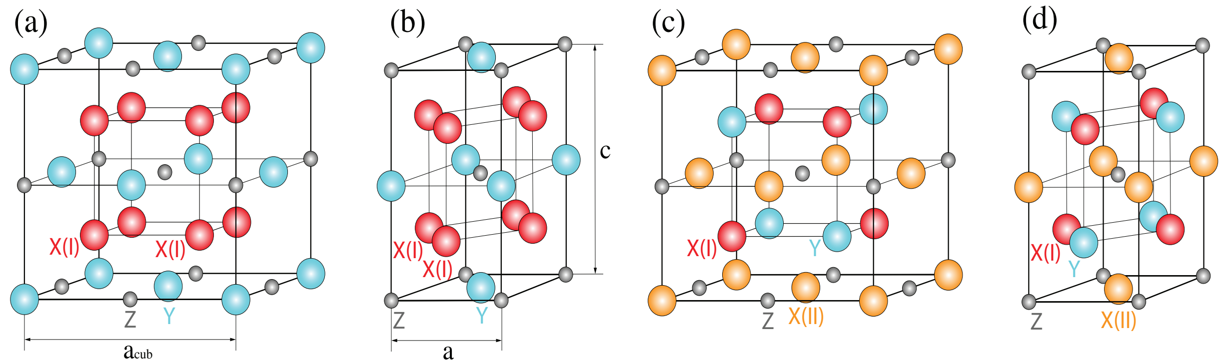

FIG. 1: (a) regular and (c) inverse cubic Heusler structure. (b) regular and (d) inverse tetragonal Heusler structure.

beled as X(I)] is located on site I in one xy-plane with Y atom (cyan), while another X atom [orange, labeled as X(II)] is located on site II in one xy-plane with Z atom (grey).

Regular [Fig 1(b)] and inverse [Fig 1(d)] tetragonal Heusler structures can be obtained from regular and inverse cubic structures, correspondingly, by stretching (or compressing) parent cubic structure along the z-axis. Tetragonal unit cells shown on Fig 1(b) and Fig 1(d) are rotated on 45^o around z-axis relative to the parent cubic structures shown on Fig 1(a) and Fig 1(c), correspondingly. (Note that only part of atoms from Fig 1(a) and Fig 1(c) are shown on Fig 1(b) and Fig 1(d).) Lattice constant a_{cub} of the cubic Heusler is shown on Fig 1(a) and lattice constants a and c of the tetragonal Heusler are shown on Fig 1(b). For characterization of the tetragonal unit cell we use dimensionless parameter $c' = c/(2a)$ that is equal to $1/\sqrt{2}$ for the cubic structure, and vary between 0.8 and 1.1 for most of the tetragonal Heuslers we found (see Table I). Note that for $c' = 1$ tetragonal structure would become the *fcc* structure if all four atoms of the compound could be considered as equivalent.

B. Computational details

We performed DFT calculations for both the regular and inverse structures (with various magnetic configurations) of 286 Heusler compounds[15] using the VASP program[16] with PAW potentials[17,18] and PBE GGA/DFT functional[19]. In particular, we performed calculations for Heusler compounds X_2YZ with X={Mn,Fe,Co} and YZ={Mn,Fe,Co,Ni,Cu}{Al,Ga,Si,Ge,Sn,Sb}, and YZ={Mo,Ru,Rh,Pd,W,Os,Ir,Pt}{Ga,In,Ge,Sn,Sb}, X={Ru,Rh,Pd} and YZ={Mn,Fe,Co}{Ga,In,Ge,Sn,Sb}, X=Ni and YZ={Mn,Fe,Co}{Al,Ga,Si,Ge,Sn,Sb}, X=Mn and YZ={Fe,Co,Ni,Cu}{In}, and compounds X_3Z with X={Mn,Fe,Co} and Z={In,P,As}. For binary compounds X_3Z we also considered hexagonal structures with X atoms forming a Kagome lattice in a plane with a Z atom in the center of the hexagon (see, e.g., Ref[20] for figure of the hexagonal structure).

The results of calculations are summarized in Table I for 116 compounds with tetragonal lowest energy configuration and $E_{21} \geq 0.05eV$, where phase stability energy, E_{21}, is defined as the difference between the total energy of the second lowest energy configuration and the total energy of the lowest energy configuration. The remaining 170 compounds that are not included in Table I ether have cubic or hexagonal lowest energy configuration or tetragonal lowest energy configuration with low phase stability energy, $E_{21} < 0.05eV$. (See Ref.[15] for explanation of such a large share of stable tetragonal compounds - 116 - out of 286 studied compounds.) The convergence of presented results was verified by varying the number of divisions in reciprocal space from $10\times10\times10$ to $18\times18\times18$ and the energy cut-off from 400eV to 520eV.

The MCA energy, K_{mc}, of tetragonal Heusler compounds is calculated as the difference between total energies of states with magnetization along the x-axis and the z-axis, $K_{mc} = E_{(100)} - E_{(001)}$, where positive K_{mc} means out-of-plane magnetization. We also calculated the volume magnetic anisotropy, $K_v = K_{mc} - K_{sh}$, where $K_{sh} = \mu_0 M_s^2 V/2$, is the shape anisotropy energy of thin film per unit cell of volume V, and M_s is saturation magnetisation and μ_0 is vacuum permeability.

We calculated Curie temperature, T_C, within the standard mean-field approximation (MFA)[21] using the exchange constants, J_{ij}, of the effective Heisenberg Hamiltonian (i and j are the site indexes). In this approach T_C can be estimated as $k_B T_C = 2/3 J_{max}$, where J_{max} is the maximal eigenvalue of the (4×4) $J^{\mu\nu}$ matrix, with $J^{\mu\nu} = \sum_{j\in\nu} J_{0j}$. Here 0 is fixed index in sublattice μ and sum is taken over sites in sublattice ν. The exchange constants J_{ij} were calculated by using the Green's function approach implemented within the LMTO-ASA framework[22,23].

For each stable tetragonal compound Table I shows the lattice parameters a and c', the lowest and the second lowest energy configurations labels s_1 and s_2, magnetic moment m, phase stability energy E_{21}, total spin polarization SP_t as well as the spin polarization of individual termination layers SP_1 and SP_2, anisotropy constants

TABLE I: Calculated lattice parameters, a and c', labels of the lowest energy configuration, s_1, and the second lowest energy configuration, s_2, the phase stability energy, E_{21}, magnetic moment, m, total spin polarization, SP_t, spin polarizations, SP_1 and SP_2, of two termination layers, anisotropy constants, K_{mc}, K_{sh}, and K_v, and the Curie temperature, T_C, for 116 stable tetragonal Heuslers with $E_{21} \geq 0.05eV$ (see text for details).

	a (Å)	c'	s_1	s_2	E_{21} (eV)	m (μ_B)	SP_t	SP_1	SP_2	K_{mc} $\frac{meV}{f.u.}$	K_{sh} $\frac{meV}{f.u}$	K_v $\frac{MJ}{m^3}$	T_C (K)
Mn_2NiAl	3.81	0.88	ti	ci	0.06	1.01	0.27	0.36	0.03	0.167	0.007	0.53	887
Mn_3Ga	3.78	0.94	t	c	0.19	1.79	-0.60	-0.67	-0.49	0.884	0.021	2.72	658
Mn_2FeGa	3.69	0.98	ti	ci	0.14	0.84	-0.58	-0.71	-0.33	0.494	0.005	1.59	751
Mn_2NiGa	3.79	0.91	ti	ci	0.12	0.99	0.66	0.70	0.54	0.162	0.007	0.51	821
Mn_3In	3.95	0.96	t	h	0.15	1.93	-0.72	-0.81	-0.53	1.218	0.021	3.24	461
Mn_2FeIn	3.89	0.98	ti	ti	0.18	0.94	-0.75	-0.63	-0.86	0.659	0.005	1.82	715
Mn_2CoIn	3.90	0.96	ti	ci	0.06	0.08	0.65	0.76	0.30	0.122	0.000	0.34	170
Mn_2NiSi	3.61	0.97	ti	ci	0.10	0.32	0.06	0.19	-0.18	0.140	0.001	0.49	548
Mn_2CuSi	3.71	0.94	tr	ci	0.19	4.92	-0.29	-0.29	-0.14	0.474	0.170	1.02	426
Mn_3Ge	3.73	0.95	t	c	0.10	1.01	-0.72	-0.77	-0.63	0.770	0.007	2.48	503
Mn_2CoGe	3.74	0.92	ti	ci	0.07	0.97	0.78	0.85	0.50	0.208	0.007	0.67	665
Mn_2NiGe	3.73	0.95	ti	ci	0.08	0.31	-0.26	-0.17	-0.47	0.135	0.001	0.44	744
Mn_2CuGe	3.77	0.95	tr	ci	0.21	5.28	-0.31	-0.30	-0.17	0.646	0.185	1.45	397
Mn_3Sn	3.93	0.95	t	h	0.17	1.04	-0.87	-0.92	-0.68	0.958	0.006	2.65	264
Mn_2CoSn	3.96	0.90	ti	ci	0.15	1.00	0.89	0.93	0.69	0.337	0.006	0.95	603
Mn_2CuSn	3.91	0.98	tr	ci	0.06	5.73	-0.30	-0.32	-0.06	0.965	0.189	2.12	421
Mn_3Sb	3.82	1.02	t	h	0.14	1.14	0.23	0.09	0.58	0.241	0.008	0.66	284
Mn_2NiSb	3.81	1.02	tr	ti	0.11	5.85	-0.47	-0.42	-0.51	0.926	0.204	2.05	132
Mn_2CuSb	3.86	1.01	tr	ti	0.27	5.45	-0.33	-0.36	-0.05	0.963	0.172	2.18	53
Mn_2RuGa	3.81	0.97	ti	ci	0.10	0.26	0.03	-0.14	0.26	0.599	0.000	1.79	1107
Mn_2RhGa	3.83	0.97	ti	ci	0.17	0.07	0.65	0.81	0.26	0.302	0.000	0.89	1112
Mn_2PdGa	3.93	0.92	ti	ci	0.10	0.92	0.46	0.63	0.00	0.021	0.005	0.05	551
Mn_2MoIn	4.09	0.88	tr	cr	0.09	3.73	0.26	0.20	0.60	1.473	0.078	3.71	477
Mn_2RuIn	3.94	1.00	ti	tr	0.21	0.30	0.17	-0.03	0.45	0.865	0.000	2.26	992
Mn_2RhIn	3.98	0.98	ti	ci	0.22	0.05	0.59	0.80	0.19	-0.002	0.000	0.00	825
Mn_2RhGe	3.85	0.94	ti	ci	0.22	0.77	-0.07	0.23	-0.66	0.019	0.004	0.04	463
Mn_2MoSn	3.86	1.08	ti	tr	0.07	0.14	-0.12	0.02	-0.31	-0.473	0.000	-1.22	768
Mn_2RuSn	3.97	0.97	ti	ci	0.21	0.00	0.91	0.96	0.77	0.431	0.000	1.14	783
Mn_2RhSn	4.03	0.93	ti	ci	0.14	0.75	-0.45	-0.20	-0.83	-0.068	0.003	-0.19	309
Mn_2PdSn	4.17	0.89	ti	ci	0.05	0.20	-0.04	0.31	-0.55	-0.074	0.000	-0.19	710
Mn_2MoSb	3.88	1.06	ti	ci	0.26	0.20	0.47	0.43	0.60	0.029	0.000	0.08	647
Mn_2RuSb	3.94	0.98	ti	ci	0.17	0.17	-0.38	-0.19	-0.74	-0.208	0.000	-0.56	321
Mn_2RhSb	4.00	0.96	ti	tr	0.16	0.00	0.45	0.51	0.13	0.106	0.000	0.28	747
Mn_2OsGa	3.80	0.98	ti	ci	0.15	0.28	0.08	0.00	0.20	3.291	0.000	9.81	929
Mn_2IrGa	3.83	0.97	ti	ci	0.27	0.07	0.57	0.73	0.23	2.760	0.000	8.11	962
Mn_2PtGa	3.90	0.94	ti	tr	0.11	0.87	0.34	0.54	-0.23	-0.210	0.005	-0.62	375
Mn_2OsIn	3.92	1.01	ti	tr	0.27	0.29	0.23	0.11	0.39	4.699	0.000	12.37	734
Mn_2IrIn	3.96	0.99	ti	tr	0.30	0.04	0.78	0.90	0.43	1.754	0.000	4.57	497
Mn_2OsGe	3.81	0.97	ti	ci	0.06	0.03	-0.91	-0.94	-0.83	2.620	0.000	7.82	476
Mn_2IrGe	3.83	0.96	ti	tr	0.25	0.51	-0.62	-0.44	-0.86	0.046	0.002	0.13	365
Mn_2OsSn	3.96	0.98	ti	ci	0.33	0.02	-0.91	-0.95	-0.77	4.047	0.000	10.65	611
Mn_2IrSn	3.99	0.96	ti	ci	0.22	0.46	-0.65	-0.45	-0.89	-0.578	0.001	-1.52	227
Mn_2WSb	3.84	1.08	ti	cr	0.23	0.06	0.49	0.44	0.59	-0.894	0.000	-2.34	603
Mn_2OsSb	3.96	0.97	ti	ci	0.24	0.17	-0.46	-0.26	-0.78	0.991	0.000	2.64	206
Fe_2CuAl	3.57	1.08	tr	ci	0.16	4.65	-0.11	-0.24	0.07	0.135	0.148	-0.04	1295
Fe_2CuGa	3.60	1.06	tr	ti	0.22	4.73	-0.14	-0.33	0.29	0.156	0.153	0.01	1238
Fe_2NiSi	3.49	1.06	tr	ci	0.12	4.68	0.20	0.09	0.39	0.248	0.164	0.30	1083
Fe_2CuSi	3.55	1.03	tr	ti	0.10	4.24	-0.66	-0.74	-0.46	0.588	0.132	1.59	675
Fe_2NiGe	3.54	1.07	tr	ci	0.16	4.83	0.04	-0.14	0.36	0.290	0.166	0.42	1081
Fe_2CuGe	3.61	1.05	tr	ti	0.15	4.59	-0.59	-0.68	-0.33	0.288	0.144	0.47	615
Fe_2MnSn	3.97	0.90	ti	ci	0.08	7.34	-0.18	-0.23	-0.04	0.773	0.323	1.28	1012
Fe_2NiSn	3.68	1.09	tr	ci	0.06	4.97	-0.18	-0.36	0.14	0.347	0.153	0.57	1077
Fe_2CuSn	3.76	1.06	tr	ti	0.11	4.87	-0.40	-0.51	0.00	-0.630	0.142	-2.19	849
Fe_2NiSb	3.70	1.09	tr	ti	0.13	5.41	-0.20	-0.40	0.13	-0.395	0.179	-1.67	1210
Fe_2PdGe	3.67	1.09	tr	ti	0.07	5.12	-0.27	-0.46	0.19	0.429	0.164	0.79	1086
Fe_2MoSb	3.78	1.08	ti	cr	0.08	1.34	0.08	-0.25	0.52	-0.336	0.010	-0.95	11
Fe_2PdSb	3.86	1.06	tr	ti	0.10	5.57	-0.21	-0.49	0.40	-0.213	0.172	-1.01	1268
Fe_2PtIn	3.97	0.96	ti	ci	0.07	5.24	-0.39	-0.50	-0.32	-1.160	0.154	-3.50	1220
Fe_2PtGe	3.68	1.10	tr	ti	0.10	5.25	-0.26	-0.46	0.26	1.487	0.170	3.85	1081
Fe_2PtSb	3.87	1.06	tr	ti	0.17	5.61	-0.28	-0.56	0.43	1.036	0.173	2.25	1317

	a (Å)	c'	s_1	s_2	E_{21} (eV)	m (μ_B)	SP_t	SP_1	SP_2	K_{mc} $\frac{meV}{f.u.}$	K_{sh} $\frac{meV}{f.u}$	K_v $\frac{MJ}{m^3}$	T_C (K)
Co_2NiAl	3.67	0.92	ti	tr	0.13	2.65	-0.52	-0.44	-0.66	-0.629	0.052	-2.40	756
Co_2NiGa	3.69	0.92	ti	tr	0.10	2.73	-0.57	-0.36	-0.74	-0.618	0.054	-2.33	721
Co_2CuGa	3.70	0.94	ti	cr	0.05	2.58	-0.65	-0.64	-0.72	-0.087	0.047	-0.45	697
Co_2CoSi	3.58	0.93	t	h	0.07	2.79	-0.66	-0.60	-0.75	-0.599	0.062	-2.48	622
Co_2NiSi	3.55	0.96	ti	tr	0.05	2.23	-0.51	-0.42	-0.65	0.347	0.039	1.15	589
Co_2CoGe	3.64	0.94	t	h	0.10	2.99	-0.72	-0.68	-0.78	-0.634	0.066	-2.48	616
Co_2CoSn	3.81	0.94	t	c	0.08	3.17	-0.76	-0.74	-0.81	-0.640	0.065	-2.17	603
Co_2NiSn	3.80	0.95	ti	tr	0.09	2.49	-0.55	-0.48	-0.68	-0.066	0.040	-0.33	554
Co_2FeSb	3.97	0.85	tr	cr	0.14	4.81	-0.18	0.02	-0.49	-0.369	0.147	-1.55	849
Co_2CoSb	3.77	0.95	t	h	0.07	2.49	-0.51	-0.41	-0.67	0.129	0.041	0.28	455
Co_2MoGa	3.80	0.92	tr	cr	0.12	0.79	-0.11	-0.10	-0.13	0.053	0.004	0.15	6
Co_2PdGa	3.82	0.92	ti	tr	0.18	2.78	-0.50	-0.35	-0.66	-0.843	0.051	-2.79	785
Co_2RhIn	3.89	0.96	ti	ci	0.10	3.47	-0.78	-0.74	-0.86	-0.653	0.072	-2.05	729
Co_2PdIn	3.93	0.95	ti	tr	0.16	2.96	-0.74	-0.65	-0.84	-0.923	0.051	-2.71	758
Co_2RhGe	3.78	0.92	ti	ci	0.23	2.69	-0.67	-0.53	-0.81	-0.734	0.049	-2.52	624
Co_2PdGe	3.76	0.96	ti	tr	0.17	2.49	-0.59	-0.47	-0.72	0.230	0.041	0.60	653
Co_2MoSn	4.07	0.84	tr	cr	0.07	2.12	0.62	0.45	0.78	0.009	0.027	-0.05	97
Co_2RhSn	3.92	0.93	ti	ci	0.23	2.87	-0.72	-0.66	-0.81	-0.654	0.049	-2.01	664
Co_2PdSn	3.89	0.97	ti	tr	0.15	2.54	-0.55	-0.50	-0.65	-0.025	0.038	-0.18	610
Co_2RuSb	3.87	0.95	ti	ci	0.17	2.43	-0.37	-0.24	-0.57	0.192	0.036	0.45	446
Co_2RhSb	3.88	0.95	ti	tr	0.25	2.34	-0.62	-0.53	-0.76	0.403	0.033	1.07	536
Co_2WGa	3.88	0.87	tr	cr	0.13	1.07	0.49	0.48	0.51	0.812	0.008	2.54	64
Co_2OsGa	3.70	0.97	tr	ti	0.06	0.57	-0.49	-0.47	-0.50	-0.620	0.002	-2.03	0
Co_2IrGa	3.77	0.95	ti	ci	0.05	3.09	-0.63	-0.56	-0.73	-3.306	0.063	-10.61	557
Co_2PtGa	3.80	0.94	ti	tr	0.18	2.82	-0.69	-0.68	-0.75	-3.745	0.052	-11.79	748
Co_2IrIn	3.82	1.02	ti	tr	0.11	3.37	-0.76	-0.71	-0.84	-2.828	0.067	-8.16	581
Co_2PtIn	3.90	0.98	ti	tr	0.14	3.01	-0.80	-0.78	-0.86	-2.794	0.053	-7.84	715
Co_2IrGe	3.76	0.95	ti	ci	0.24	2.51	-0.54	-0.41	-0.69	-2.731	0.042	-8.80	528
Co_2PtGe	3.76	0.97	ti	tr	0.16	2.44	-0.58	-0.53	-0.68	-0.404	0.039	-1.38	648
Co_2WSn	4.07	0.84	tr	cr	0.11	1.76	0.14	-0.11	0.41	-4.368	0.018	-12.41	43
Co_2IrSn	3.88	0.97	ti	tr	0.20	2.79	-0.66	-0.59	-0.76	-2.963	0.046	-8.51	596
Co_2PtSn	3.89	0.98	ti	tr	0.11	2.52	-0.55	-0.52	-0.66	0.206	0.037	0.47	624
Co_2WSb	3.76	1.07	ti	tr	0.05	1.12	0.52	0.43	0.67	-0.664	0.007	-1.89	5
Co_2OsSb	3.86	0.97	ti	ci	0.23	2.19	-0.22	-0.17	-0.34	-2.806	0.029	-8.14	428
Co_2IrSb	3.86	0.97	ti	tr	0.27	2.34	-0.43	-0.37	-0.55	-0.801	0.033	-2.40	550
Pd_2FeGa	3.96	0.93	tr	cr	0.09	3.22	-0.35	-0.14	-0.60	0.041	0.061	-0.06	457
Pd_2CoGa	3.92	0.93	tr	cr	0.21	1.94	-0.50	-0.35	-0.67	-0.383	0.022	-1.16	341
Pd_2FeIn	4.09	0.93	tr	cr	0.06	3.20	-0.39	-0.28	-0.62	0.257	0.054	0.51	543
Pd_2CoIn	4.03	0.95	tr	cr	0.21	1.94	-0.39	-0.19	-0.62	-0.483	0.020	-1.30	261
Pd_2FeGe	3.91	0.97	tr	cr	0.10	3.12	-0.70	-0.26	-0.86	0.150	0.057	0.26	245
Pd_2CoGe	3.90	0.95	tr	ti	0.11	1.71	-0.67	-0.46	-0.80	1.389	0.017	3.90	259
Pd_2CoSn	4.03	0.95	tr	ti	0.10	1.61	-0.71	-0.46	-0.84	1.064	0.014	2.70	217
Pd_2CoSb	4.12	0.89	ti	ci	0.05	1.25	-0.44	-0.56	-0.18	-0.060	0.008	-0.18	0
Rh_2FeGe	4.01	0.85	tr	cr	0.21	3.83	-0.49	-0.09	-0.78	-0.898	0.090	-2.89	516
Rh_2CoGe	3.95	0.87	tr	cr	0.19	2.22	-0.57	-0.13	-0.80	-0.754	0.031	-2.34	487
Rh_2FeSn	4.16	0.85	tr	cr	0.19	3.89	-0.61	-0.29	-0.83	-0.985	0.083	-2.80	503
Rh_2CoSn	4.07	0.89	tr	cr	0.21	2.30	-0.61	-0.22	-0.84	-0.621	0.030	-1.75	511
Rh_2MnSb	4.15	0.87	tr	cr	0.20	4.17	0.00	0.07	-0.04	-0.469	0.094	-1.46	336
Rh_2FeSb	4.05	0.91	tr	cr	0.37	3.38	-0.42	0.08	-0.76	-0.164	0.064	-0.60	472
Rh_2CoSb	4.01	0.92	tr	ti	0.44	2.05	-0.22	0.23	-0.59	0.685	0.024	1.79	48
Ru_2CoGa	3.72	1.02	ti	cr	0.11	1.06	-0.48	-0.49	-0.50	-0.064	0.007	-0.22	34
Ru_2CoIn	3.89	0.99	ti	cr	0.22	1.28	-0.46	-0.50	-0.43	-0.009	0.009	-0.05	80
Ru_2CoSn	3.90	0.98	ti	cr	0.07	0.04	-0.17	-0.19	-0.13	0.000	0.000	0.00	0
Ni_2FeGa	3.67	0.96	tr	cr	0.07	3.30	-0.31	-0.30	-0.44	0.084	0.077	0.02	524
Ni_2CoSi	3.60	0.92	ti	ci	0.11	0.89	-0.67	-0.69	-0.68	0.156	0.006	0.56	105
Ni_2CoGe	3.66	0.93	ti	tr	0.11	1.03	-0.68	-0.70	-0.68	0.124	0.008	0.41	94

K_{mc}, K_{sh}, and K_v, and T_C. For ternary compounds labels $s_1, s_2 = tr, ti, cr$, or ci represent tetragonal regular, tetragonal inverse, cubic regular, or cubic inverse phase, correspondingly. For binary compounds $s_1, s_2 = t, c$, or h represent tetragonal, cubic or hexagonal phase, correspondingly. Since only stable tetragonal compounds are presented in Table I, s_1 always indicates tetragonal phase, $s_1 = tr, ti$, or t. Anisotropy constants K_{mc} and K_{sh} are shown in Table I in $\frac{meV}{f.u.}$ units, while $K_v = K_{mc} - K_{sh}$ is converted from $\frac{meV}{f.u.}$ to $\frac{MJ}{m^3}$ units. Positive K_v indicates that this compound has PMA. Three values of the spin polarisation shown in Table I - SP_t, SP_1, and SP_2 - are defined as $\frac{DOS_1 - DOS_2}{DOS_1 + DOS_2}$, where $DOS_{1/2}$ is density of states at the Fermi energy, E_F, of majority/minority electrons

TABLE II: The values of E_z calculated by GGA, LDA, and QSGW methods are shown for 28 tetragonal Heusler compounds.

		E_z^{GGA} (eV)	E_z^{LDA} (eV)	E_z^{GW} (eV)			E_z^{GGA} (eV)	E_z^{LDA} (eV)	E_z^{GW} (eV)			E_z^{GGA} (eV)	E_z^{LDA} (eV)	E_z^{GW} (eV)			E_z^{GGA} (eV)	E_z^{LDA} (eV)	E_z^{GW} (eV)			E_z^{GGA} (eV)	E_z^{LDA} (eV)	E_z^{GW} (eV)
Mn_3Ge	↓	-0.08	-0.05	-0.03	Mn_2CuSi	↓	0.41	0.33	0.41	Mn_2OsGe	↓	-0.05	-0.03	0.16	Fe_2NiSb	↓	0.11	0.06	0.21	Fe_2PdGe	↓	-0.36	-0.41	-0.28
Mn_3Sn	↓	-0.22	-0.17	0.20	Mn_2CuGe	↓	0.42	0.49	0.17	Ni_2CoGe	↓	0.00	0.00	0.08	Fe_2CuAl	↑	0.06	0.17	0.11	Fe_2PdSb	↓	0.18	0.14	0.26
Mn_3Sb	↓	-0.10	-0.12	0.29	Mn_2CuSn	↓	0.08	0.15	0.00	Fe_2MnSn	↓	0.24	0.08	0.23	Fe_2CuAl	↓	-0.22	-0.31	-0.12	Fe_2PtGe	↓	-0.31	-0.34	-0.16
Mn_2CoSn	↓	-0.05	-0.03	-0.02	Mn_2MoSn	↑	-0.16	-0.16	-0.27	Fe_2NiSi	↓	0.27	0.18	0.37	Fe_2CuGa	↑	-0.09	0.03	0.00	Fe_2PtSb	↓	0.09	0.09	0.16
Mn_2NiSi	↑	0.16	0.06	-0.14	Mn_2MoSb	↓	-0.44	-0.40	-0.41	Fe_2NiGe	↓	0.39	0.28	-0.29	Fe_2CuGa	↓	-0.06	-0.14	0.00	Co_2NiGa	↓	0.00	0.00	-0.05
Mn_2NiGe	↑	-0.23	0.11	0.09	Mn_2WSb	↓	-0.58	-0.49	-0.56	Fe_2NiSn	↓	-0.30	-0.28	-0.34	Fe_2MoSb	↓	0.14	0.12	0.00	Co_2PdGa	↓	0.00	0.00	-0.03

calculated for the whole system, projected to two-atom termination layer (xy-plane) that does not contains atom Z, or to two-atom termination layer that contains atom Z, correspondingly.

C. Compounds with expected large TMR due to Brillouin zone spin filtering effect

The so-called Brillouin zone (BZ) spin filtering effect[13] in a ME/MgO/ME MTJ system occurs if magnetic electrode (ME) has states at the Fermi energy, E_F, along the Γ-Z line in one spin channel, σ_1, and does not have such states in another spin channel, σ_2. [Γ-Z line in BZ is the line along k_z direction with in-plane wavevector $\mathbf{k}_{||} = (k_x, k_y) = 0$.] It is well known[24,25] that the smallest (at given $\mathbf{k}_{||}$) attenuation constant $\gamma(\mathbf{k}_{||})$ of MgO for evanescent states propagating along the z-direction with energies within the MgO band gap reaches a minimum at $\mathbf{k}_{||} = 0$. When $|\mathbf{k}_{||}|$ increases, $\gamma(\mathbf{k}_{||})$ increases as $\gamma(\mathbf{k}_{||}) = \gamma_0 + \alpha \mathbf{k}_{||}^2$ (with $\alpha > 0$). Therefore, at $E = E_F$, the evanescent states of ME in σ_1 spin channel that propagate along z direction with $\mathbf{k}_{||} = 0$ will decay inside MgO as $e^{-\gamma_0 z}$, while evanescent states in σ_2 spin channel will decay as $e^{-(\gamma_0 + \alpha \mathbf{k}_{||}^2) z}$, with $|\mathbf{k}_{||}| > 0$ since σ_2 channel does not have states at E_F with $\mathbf{k}_{||} = 0$. As a result the TMR increases exponentially with increasing MgO thickness, d_{MgO}: $TMR \propto \exp(2\alpha \tilde{\mathbf{k}}_{||}^2 d_{MgO})$, where $\tilde{\mathbf{k}}_{||}$ is the shortest vector $\mathbf{k}_{||}$ for which ME has states in the σ_2 spin channel at E_F. Such dependance on d_{MgO} is much stronger than the $TMR \propto d_{MgO}^n$ dependance arising from the symmetry filtering effect[24,25], where the power factor n can only take three values $n = 0, 1, 2$ for MTJ systems with square symmetry in xy plane[26].

Table II shows the values of $E_z = E_c - E_F$ for 26 compounds that have band gap along Γ-Z line ($|E_z| > 0$) in only one spin channel, and for Fe_2CuAl and Fe_2CuGa that have band gap ($|E_z| > 0$) in both spin channels. Here E_c is the closest to E_F energy among energies of states in corresponding spin channel with $\mathbf{k}$ along the Γ-Z line. The value of $|E_z|$ characterizes the strength of the BZ filtering effect since larger $|E_z|$ leads to larger value of $\tilde{\mathbf{k}}_{||}$ and, therefore, to faster TMR increase with d_{MgO}. Also, large values of $|E_z|$ make the existence of the BZ filtering effect less susceptible to the details of calculations (choice of the DFT functional, variations of the lattice constants, etc) as well as to the experimental conditions (effects of disorder, finite temperature, finite applied bias, etc).

The majority (minority) spin channel with $|E_z| > 0$ is indicated in Table II by an up (down) arrow. Positive (negative) E_z indicates that the band closest to E_F is located above (below) E_F. For each compound E_z was calculated by three different methods: the pseudo-potential PAW approach implemented in VASP program with PBE GGA/DFT functional, the full-potential all-electron LMTO approach[27] with Barth-Hedin LDA/DFT functional[28], and the QSGW method that is known to describe band gaps and other properties of materials with moderate e-e correlations significantly better than DFT[29–31]. Three values of E_z are indicated as E_z^{GGA}, E_z^{LDA}, and E_z^{GW}, correspondingly in Table II. The majority and minority bands along the Γ-Z line calculated by the GGA/DFT, LDA/DFT, and QSGW methods are shown for 28 compounds in Figs. 2-5 by red, green, and blue colors, correspondingly.

Table II shows that for Mn_2CuSn, Fe_2CuGa, and Fe_2MoSb compounds $|E_z^{GGA}| > 0$ and $|E_z^{LDA}| > 0$, while the gap along Γ-Z closes in QSGW, $|E_z^{GW}| = 0$. On the other hand for Ni_2CoGe, Co_2NiGa, and Co_2PdGa compounds $|E_z^{GGA}| = |E_z^{LDA}| = 0$, while the gap along Γ-Z line opens in QSGW, $|E_z^{GW}| > 0$. Thus, beyond DFT calculations are necessary in order to accurately estimate E_z. Note that for one of the most studied tetragonal Heusler compound, Mn_3Ge, the QSGW value $|E_z^{GW}| = 0.03eV$ is significantly smaller than GGA value $|E_z^{GGA}| = 0.08eV$. Therefore, high TMR values predicted previously by DFT calculations in Mn_3Ge/MgO/Mn_3Ge MTJ[9,12,32] are expected to be significantly lower if calculated by more accurate beyond DFT methods.

Table II shows that there are 17 compounds with relatively large $|E_z^{GW}| > 0.15eV$. These compound are expected to exhibit large TMR in MTJ devices. Among these 17 compounds 13 have PMA ($K_v > 0$) and 10 have strong PMA with $K_v > 0.5MJ/m^3$: Mn_3Sn, Mn_3Sb, Mn_2CuSi, Mn_2CuGe, Mn_2OsGe, Fe_2MnSn, Fe_2NiSn, Fe_2PdGe, Fe_2PtGe, and Fe_2PtSb. These 10 compound constitute our 'best' candidates for STT-MRAM applications identified in present paper. Note, that five Fe-based compound in this list have high $T_C > 1000K$ (see Table I).

D. Compounds with expected large TMR due to large spin polarization

Large spin polarization of bulk Heusler compound also could result in enhanced TMR values. We identified

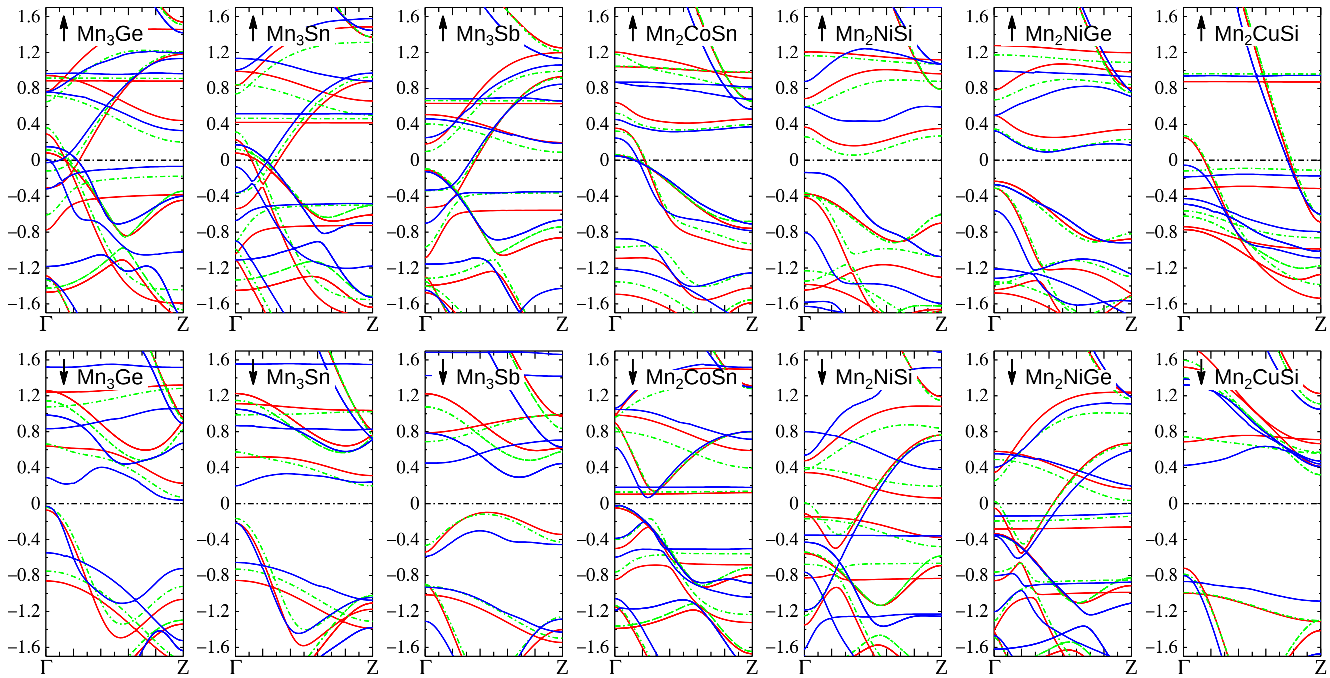

FIG. 2: Majority (↑) and minority (↓) bands of Mn_3Ge, Mn_3Sn, Mn_3Sb, Mn_2CoSn, Mn_2NiSi, Mn_2NiGe, and Mn_2CuSi along the Γ-Z line. GGA, LDA, and QSGW bands are shown by the red, green, and blue colors. Vertical scale is $E - E_F$ (eV).

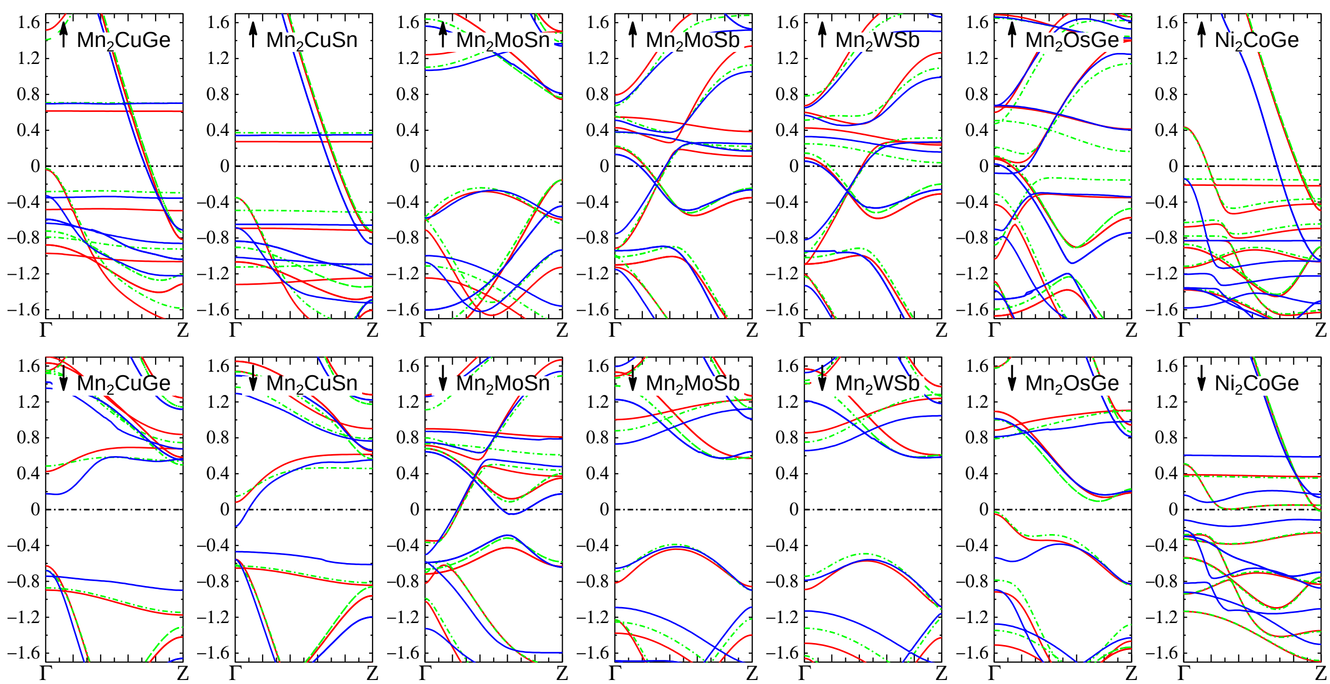

FIG. 3: Majority (↑) and minority (↓) bands of Mn_2CuGe, Mn_2CuSn, Mn_2MoSn, Mn_2MoSb, Mn_2WSb, Mn_2OsGe, and Ni_2CoGe along the Γ-Z line. GGA, LDA, and QSGW bands are shown by the red, green, and blue colors. Vertical scale is $E - E_F$ (eV).

11 compounds - Mn_3In, Mn_2FeIn, Mn_3Ge, Mn_2CoGe, Mn_3Sn, Mn_2CoSn, Mn_2RuSn, Mn_2IrIn, Mn_2OsGe, Mn_2OsSn, and Pd_2CoS - in Table I that have large total spin polarization, $|SP_t| > 0.7$ and, simultaneously, PMA with $K_v > 0.6 MJ/m^3$. These 11 compounds constitute our 'second best' list of candidates for STT-MRAM applications. Eight compounds from this list have very strong PMA with $K_v \geq 1.8 MJ/m^3$ and nine compounds have $T_C > 460K$. Note that the sign of the spin polarization is the same for both termination layers for these 11 com-

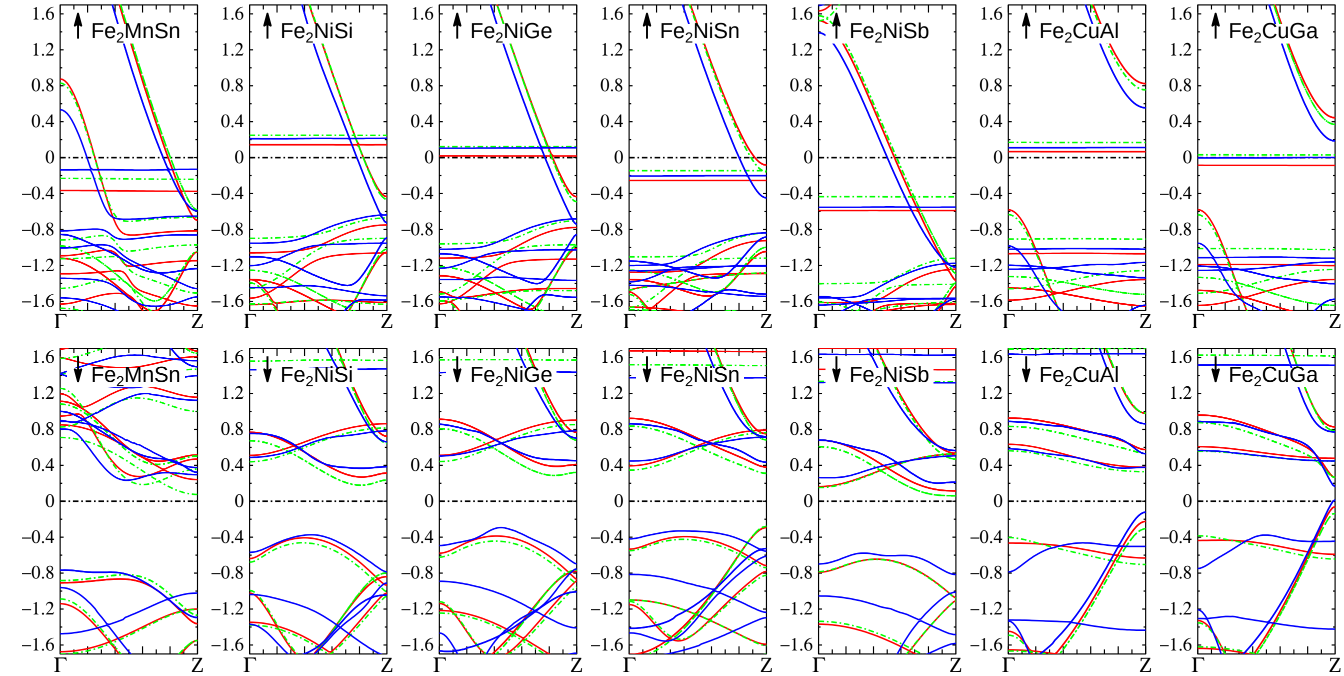

FIG. 4: Majority (↑) and minority (↓) bands of Fe_2MnSn, Fe_2NiSi, Fe_2NiGe, Fe_2NiSn, Fe_2NiSb, Fe_2CuAl, and Fe_2CuGa along the Γ-Z line. GGA, LDA, and QSGW bands are shown by the red, green, and blue colors. Vertical scale is $E - E_F$ (eV).

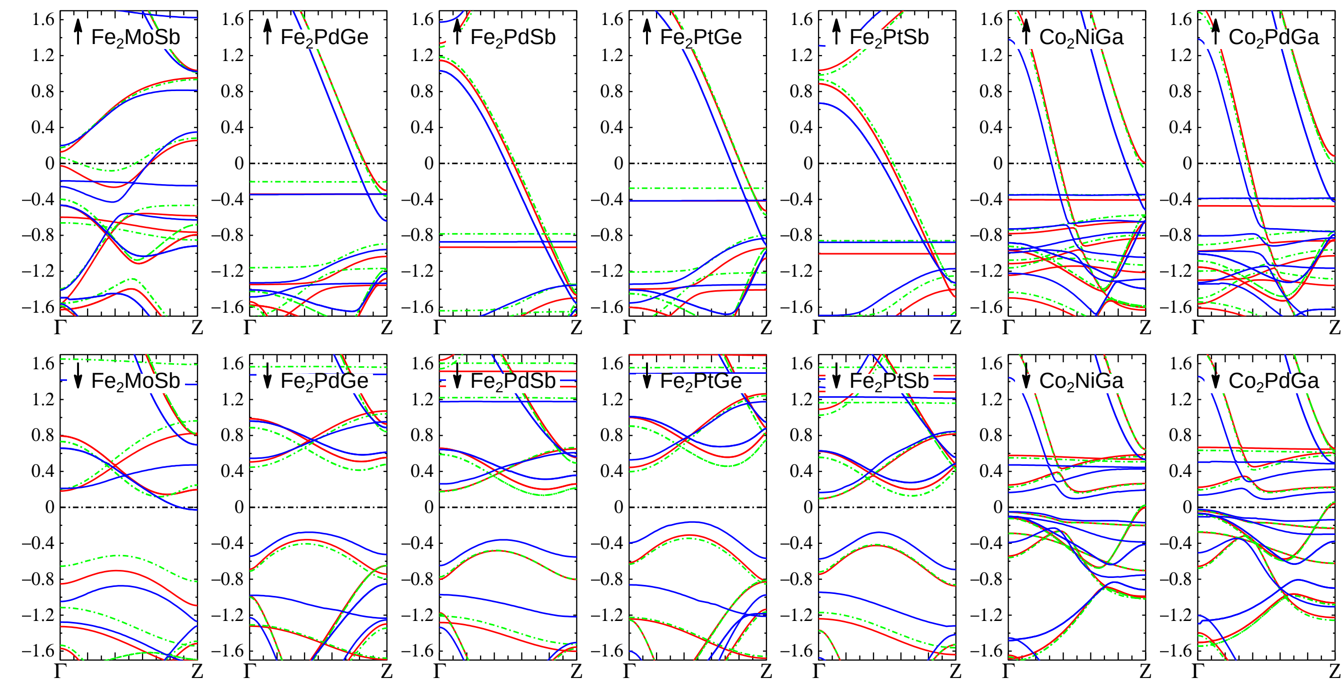

FIG. 5: Majority (↑) and minority (↓) bands of Fe_2MoSb, Fe_2PdGe, Fe_2PdSb, Fe_2PtGe, Fe_2PtSb, Co_2NiGa, and Co_2PdGa along the Γ-Z line. GGA, LDA, and QSGW bands are shown by the red, green, and blue colors. Vertical scale is $E - E_F$ (eV).

pounds (see Table I) which is important since, as was discussed in[12], in real devices both terminations can be randomly realized at the ME/MgO interface. If the signs of SP_1 and SP_2 were different, the spin polarization of the tunneling current in areas with different terminations would have different sign, thereby reducing total TMR.

Two Heusler compounds - Mn_3Sn and Mn_2OsGe - belong to both lists since they simultaneously have large spin polarization and BZ filtering conditions. Unfortunately, both effects tend to cancel each other for these

TABLE III: The experimental (c^{ex}, m^{ex}, K_v^{ex}) and calculated (c^{th}, m^{th}, K_v^{th}) values of the lattice constant, c, magnetic moment, m, and anisotropy constant, K_v, for 17 measured Heusler compounds. s^{ex} and s^{th} label experimentally found and the lowest-energy DFT-calculated structures (except for Fe_2MnGa where DFT results are shown for tetragonal phase that is 0.03 eV higher in energy than cubic one). The symbol ">" in some of experimental K_v^{ex} means that shown value is a lower bound for K_v^{ex}.

	s^{ex}	c^{ex} (Å)	m^{ex} $\frac{emu}{cm^3}$	K_v^{ex} $\frac{MJ}{m^3}$	s^{th}	c^{th} (Å)	m^{th} $\frac{emu}{cm^3}$	K_v^{th} $\frac{MJ}{m^3}$		s^{ex}	c^{ex} (Å)	m^{ex} $\frac{emu}{cm^3}$	K_v^{ex} $\frac{MJ}{m^3}$	s^{th}	c^{th} (Å)	m^{th} $\frac{emu}{cm^3}$	K_v^{th} $\frac{MJ}{m^3}$		s^{ex}	c^{ex} (Å)	m^{ex} $\frac{emu}{cm^3}$	s^{th}	c^{th} (Å)	m^{th} $\frac{emu}{cm^3}$
Mn_3Ge	tet	7.2	130	> 0.45	tet	7.09	190	2.48	Mn_2WSb	tet		250	> 0.00	tet	8.29	9	-2.34	Mn_3Si	cub	5.7	0	cub	5.64	206
Mn_3Sn	tet	7.6	150	> 0.52	tet	7.47	167	2.65	Fe_2MnGa	tet	7.0	650	0.32	tet	6.51	1335	0.30	Co_2MnAl	cub	5.7		cub	5.70	803
Mn_2FeGa	tet	7.2	300	> 1.05	tet	7.23	158	1.59	Ni_2CoGe	tet	7.1	150	> 0.00	tet	6.81	209	0.41	Co_2MnGe	cub	5.8	1000	cub	5.74	979
Mn_2CoSn	tet	6.4	350	0.26	tet	7.13	166	0.95	Rh_2FeSb	tet	7.0	300	> 0.15	tet	7.37	518	-0.60	Co_2MnSi	cub	5.6		cub	5.63	1040
Mn_2CuSb	tet	6.5	120	0.06	tet	7.80	870	2.18	Rh_2CoSb	tet	7.1	200	> 0.70	tet	7.38	320	1.79	Co_2FeAl	cub	5.6		cub	5.70	997
Mn_2RuSn	tet	7.3	175	> 0.00	tet	7.70	0	1.14										Ni_2MnGe	cub	5.8	660	cub	5.81	742

compounds. For small d_{MgO} (when effect of BZ filtering is small) the tunneling (inside MgO barrier) spin polarization for these compounds is expected to be dominated by the spin polarization of bulk Heuslers and have negative sign, while for large d_{MgO} the sign of the tunneling spin polarization should switch to positive due to increasing role of the BZ filtering effect.

We note that for ideal junctions the candidate materials from the 'best' list should have higher priority for experimental study as compared to the materials from the 'second best' list since TMR should grow exponentially with d_{MgO} for MTJs with electrodes from the 'best' list due to the BZ filtering effect, while the spin polarization induced enhancement of the TMR for MTJs with electrodes from the 'second best' list is not expected to vary much when d_{MgO} increases. On the other hand, the BZ filtering effect relies on existence of a well-defined surface Brillouin zone and in real devices (with lattice mismatch and disorder) the TMR enhancement due to the BZ filtering effect could be suppressed. The spin polarization induced enhancement of the TMR is less sensitive to the disorder and lattice mismatch. Therefore, both the 'best' list and the 'second best' list of candidate materials should be experimentally explored since the winner material could belong to any of these lists.

III. EXPERIMENTAL IDENTIFICATION OF TETRAGONAL HEUSLER COMPOUNDS WITH PERPENDICULAR MAGNETIC ANISOTROPY

We performed experimental measurements for 32 Heusler compounds. 20-30 nm thick films of these Heusler compounds were prepared by either dc-magnetron sputtering or ion-beam deposition in an ultra-high vacuum chamber (base pressure 4×10^{-10} Torr). Various buffer layers of $Si/SiO_2/TaN/IrM_3$, $Si/SiO_2/TaN/IrM_3/TaN$, MgO(001) MgO(001)/Cr, MgO(001)/Cr/Ir, $MgO(001)/Cr/IrMn_3$ were used to reduce lattice mismatch between Heusler compounds and the substrate. Each Heusler compound was grown at several different substrate temperature, typically 100^oC - 600^oC, and magnetic properties of them were measured by Quantum Design superconducting quantum interference device vibrating sample magnetometer (SQUID-VSM) in magnetic fields of up to ± 7 T. More details on the experimental set-up can be found in[12].

Comparison of the experimental results with theoretical predictions for 17 compounds are presented in Table III. Experimental measurements confirm stable tetragonal phase for 10 compounds that are predicted to be tetragonal and stable cubic phase for 6 compounds that are predicted to be cubic. Fe_2MnGa was found to be tetragonal in experiment, while predicted to be 'unstable' cubic in theory (tetragonal phase of Fe_2MnGa is only 0.03 eV higher in energy than cubic phase[15]). Note that 9 out of 11 tetragonal compounds in Table III have PMA in both the experiment and theory (exceptions are Mn_2WSb and Rh_2CoSb where $K_v^{th} < 0$, but $K_v^{ex} > 0$).

Remaining 15 out of 32 measured compounds include Co_2NiGe, Co_2RhSb, Mn_2NiSb, Mn_2CuSn, Fe_2CuAl, Co_3Sn, Co_3Sb, Co_3Ge, Fe_2CuSn, Mn_2CuSi, Co_2IrSb, Ru_2CoGa, Mn_2PtSb, Fe_2PtSb, Mn_2OsSn. All these compounds were predicted to have tetragonal phase by DFT calculations but were found to be cubic in experiment. We attribute this discrepancy to the effects of disorder that favour high-symmetry cubic phase. Since DFT calculations assume zero temperature, the finite temperature effects could also contribute to this discrepancy.

Despite disagreement between theoretical predictions and experimental results for some studied compounds, experimental confirmation of tetragonally for 10 out of 26 measured compounds that were predicted to be tetragonal by the theory shows that DFT calculations for ideal systems (without taking into account disorder and finite temperature effects) can still correctly predict tetragonally in significant share of studied cases. Moreover, for majority of found tetragonal compounds (9 out of 11) theory also correctly predicted PMA.

IV. CONCLUSION

In conclusion, we performed DFT calculation for 286 Heuslers in cubic, tetragonal and hexagonal phases, and identified 116 stable tetragonal compounds. Out of these 116 materials we identified 19 potential candidates for electrodes for STT-MRAM MTJ devices. These 19 compounds simultaneously have PMA (with high $K_v > 0.9 MJ/m^3$ for 15 of these materials) and expected to have enhanced TMR ether due to the strong BZ filtering effect ($|E_z| > 0.15eV$) or due to the high spin polarization ($|SP_t| > 0.7$). The QSGW calculations of the band structure preformed for 28 stable tetragonal compounds that satisfy the BZ filtering conditions show that beyond DFT methods are needed to accurately evaluate the strength (and even existence) of the BZ filtering effect.

We performed experimental measurements for 32 Heusler compounds. To the best of our knowledge majority of the tetragonal compounds presented in Table III are experimentally identified as tetragonal compound with PMA for the first time (exceptions are known tetragonal compounds Mn_3Ge[7], Mn_2FeGa and Fe_2MnGa[33]). Our experimental results show that DFT calculations can correctly predict both tetragonally and PMA in significant share of studied cases. Therefore, one can expect that experimental measurements for Heusler compounds theoretically predicted to be tetragonal with PMA in the present work (as well as in further theoretical studies) will result in experimental identification of significant number of stable tetragonal Heusler compounds with PMA suitable for spintronics applications.

S.F. acknowledges the CNMS User support by Oak Ridge National Laboratory Division of Scientific User facilities. S.F. thanks Oleg Mryasov for useful discussions.

* Electronic address: `svfaleev@us.ibm.com`
† Electronic address: `stuart.parkin@mpi-halle.mpg.de`

1 S. Ikeda *et al.*, Nat. Mater. **9**, 721 (2010).
2 H. Sato *et al.* Appl. Phys. Lett. **105**, 062403 (2014).
3 S. S. P. Parkin, US patent 8,008,097 (2003).
4 S. S. P. Parkin *et al.*, Nat. Mater. **3**, 862 (2004).
5 T. Graf, C. Felser, and S. S. P. Parkin, Prog. Solid State Chem. **39**, 1 (2011).
6 B. Balke, G. H. Fecher, J. Winterlik, and C. Felser, Appl. Phys. Lett. **90**, 152504 (2007).
7 H. Kurt *et al.*, Appl. Phys. Lett. **101**, 132410 (2012).
8 A. Sugihara, S. Mizukami, Y. Yamada, K. Koike, and T. Miyazaki, Appl. Phys. Lett. **104**, 132404 (2014).
9 S. Mizukami *et al.*, Appl. Phys. Expr **6**, 123002 (2013).
10 M. Li, X. Jiang, M. G. Samant, C. Felser, and S. S. P. Parkin, Appl. Phys. Lett. **103**, 032410 (2013).
11 A. Köhler, I. Knez, D. Ebke, C. Felser, and S. S. P. Parkin, Appl. Phys. Lett. **103**, 162406 (2013).
12 J. Jeong, Y. Ferrante, S. V. Faleev, M. G. Samant, C. Felser, and S. S. P. Parkin, Nat. Commun. **7**, 10276 (2016)
13 S. V. Faleev , S. S. P. Parkin, and O. N. Mryasov, Phys. Rev B **92**, 235118 (2015).
14 J. Akerman, Science, **308**, 508 (2005).
15 S. V. Faleev, Y. Ferrante, J. Jeong , M. G. Samant, B. Jones, and S. S. P. Parkin, Phys. Rev. Applied 7, 034022 (2017).
16 G. Kresse and J. Furthmuller, Phys. Rev. B **54**, 11169 (1996).
17 P. E. Blochl, Phys. Rev. B **50** 17953 (1994).
18 G. Kresse and D. Joubert, Phys. Rev. B **59**, 1758 (1999).
19 J. P. Perdew *et al.*, Phys. Rev. Lett. **77**, 3865 (1996).
20 D. Zhang, *et al.*, J. Phys.: Condens. Matter **25**, 206006 (2013).
21 A. I. Liechtenstein *et al.*, J. Magn. Magn. Materials **67**, 65 (1987).
22 O. K. Andersen and O. Jepsen, Phys. Rev. Lett. **53**, 2571 (1984).
23 M. van Schilfgaarde and W. R. L. Lambrecht, in *Tight-Binding Approach to Computational Materials Science*, ed. by L. Colombo, *et al.*, MRS Proceedings **491** (1998).
24 W. H. Butler *et al.*, Phys. Rev. B **63**, 054416 (2001).
25 J. Mathon and A. Umerski, Phys. Rev. B **63**, 220403(R) (2001).
26 S. V. Faleev, O. N. Mryasov, and S. S. P. Parkin, Phys. Rev. B **94**, 174408 (2016).
27 M. Methfessel *et al.*, Lecture Notes in Physics, **535**. H. Dreysse, ed. (Springer-Verlag, Berlin) 2000
28 U. von Barth and L. Hedin, J. Phys. C: Solid State Phys. **5** 1629 (1972).
29 S. V. Faleev, M. van Schilfgaarde, and T. Kotani, Phys. Rev. Lett. **93**, 126406 (2004)
30 M. van Schilfgaarde, T. Kotani, and S. V. Faleev, Phys. Rev. Lett. **96**, 226402 (2006)
31 T. Kotani, M. van Schilfgaarde, and S. V. Faleev, Phys. Rev. B **76**, 165106 (2007)
32 Y. Miura and M. Shirai, IEEE Trans. Magn. **50**, 1400504, (2014).
33 T. Graf, J. Winterlik, L. Muchler, G. H. Fecher, C. Felser, S. S. P. Parkin, Handbook Magn. Mater., **21**, 1 (2013).